Preprint Title Evaluation of electrosynthesized reduced graphene oxide - Ni-, Fe-, Co-based (oxy)hydroxide catalysts toward oxygen evolution reaction

Authors Karolina Cysewska, Marcin Łapiński, Marcin Zając, Jakub Karczewski, Piotr Jasiński and Sebastian Molin

Publication Date 23 Nov 2022

Article Type Full Research Paper

ORCID® iDs Karolina Cysewska - https://orcid.org/0000-0002-9503-6051; Marcin Łapiński - https://orcid.org/0000-0002-3283-2886; Piotr Jasiński - https://orcid.org/0000-0001-9249-4869; Sebastian Molin - https://orcid.org/0000-0002-8335-7632

Evaluation of electrosynthesized reduced graphene oxide - Ni-, Fe-, Co-based (oxy)hydroxide catalysts toward oxygen evolution reaction

Karolina Cysewska[1,], Marcin Łapiński[2], Marcin Zając[3], Jakub Karczewski[2], Piotr Jasiński[1], Sebastian Molin[1]*

[1] Laboratory of Functional Materials, Faculty of Electronics, Telecommunications and Informatics, Gdańsk University of Technology, ul. Narutowicza 11/12, 80-233 Gdańsk, Poland

[2] Advanced Materials Center, Institute of Nanotechnology and Materials Engineering, Faculty of Applied Physics and Mathematics, Gdańsk University of Technology, ul. Narutowicza 11/12, 80–233 Gdańsk, Poland

[3] National Synchrotron Radiation Centre SOLARIS, Jagiellonian University, ul. Czerwone Maki 98, 30-392 Cracow, Poland

* E-mail: karolina.cysewska@pg.edu.pl

ABSTRACT

In this work, the effect of the addition of graphene oxide (GO) to nickel-iron (NiFe) and cobalt-nickel-iron (CoNiFe) mixed oxide/hydroxide/(oxy)hydroxide catalysts on their morphological, structural, and oxygen evolution reaction (OER) catalytic activity is investigated. The catalysts are fabricated during two-step electrodeposition: the first step includes the deposition of GO flakes, which in the second step become reduced with simultaneous deposition of NiFe or CoNiFe. As a result, NiFe-GO and CoNiFe-GO are fabricated without any additives directly on the nickel foam substrate. A significant improvement of the OER activity was observed after combining NiFe with GO (OER overpotential $\eta(10\ mA \cdot cm^{-2})$: 210 mV) compared to NiFe (η: 235 mV) and GO (η: 320 mV)

alone. Different OER activity was observed for CoNiFe-GO. Here, the overall catalytic activity (η: 230 mV) increased compared to GO alone, however it was reduced in comparison with the CoNiFe (η: 224 mV). The latter was associated with the change in the morphology and structure of the catalysts. Further OER studies show that each of the catalysts has a specific role in influencing the process: the improvement in the OER by NiFe-GO results mainly from the structure of NiFe and the electroactive surface area of GO.

Keywords: electrocatalysts; electrodeposition; hydrogen energy; oxygen evolution reaction

1. Introduction

Nowadays, industrial production of hydrogen energy is focussed mainly on hydrocarbon reforming, which is a low-efficiency and environmentally unfriendly process [1,2]. As an alternative, water electrolysis using renewable energy sources has recently been extensively studied [3]. The main limitation to the efficiency of this process is primarily the oxygen evolution reaction (OER) due to its sluggish kinetics resulting in a high overpotential and low efficiency [4]. To overcome this problem, robust anode electrode catalyst materials are required. Since the Ru- and Pt-based catalysts used so far for OER revealed limited sources and high cost [5], studies on the other catalyst materials are being conducted.

Recently, transition-metal-based materials including nickel (Ni), iron (Fe), and/or cobalt (Co) have become promising catalysts for OER [6–10]. The materials are characterized by a relatively low cost and environmental-friendly nature [11]. Even though transition-metal-based catalysts still suffer from low surface areas [12], dissolution and aggregation of the metallic phase and metal oxides during the active OER process is possible [13]. For these reasons, Ni-, Fe- and/or Co-based catalysts have been synthesized as a hybrid catalyst with different kinds of conductive carbon materials [14–18]. Recently, graphene (Gr)/graphene oxide (GO) has attracted the attention of many researchers due to its high surface area, significant chemical stability, high electrical conductivity, and high mechanical strength [12,19]. Combining a

graphene material with Ni-, Fe- and/or Co-based oxides/hydroxides with high chemical reactivity provides both an effective electron pathway through the catalyst [20] and high specific surface area [21], which is desirable for the OER process [13]. The overall electrocatalytic performance of the hybrid electrode can also be supported by choosing a conductive and/or high surface area substrate, such as porous nickel foam [22,23].

In the literature, some research has been performed to evaluate the OER electrocatalytic performance of hybrid materials of Ni-, Fe- and/or Co-based oxides/(oxy)hydroxides and Gr and/or GO . For example, Z. Wu et al. [13] chemically fabricated metal alloys and their oxides (NiCo, CoFe) with nitrogen-doped graphene (N-rGO/NiCo-NiO-CoO, N-rGO/CoFe-Co_2FeO_4) on a glassy carbon electrode (GCE). The N-rGO/NiCo-NiO-CoO and N-rGO/CoFe-Co_2FeO_4 catalysts revealed an OER overpotential (η) of 260 mV (Tafel 72 $mV \cdot dec^{-1}$) and 320 mV (65 $mV \cdot dec^{-1}$) determined at 10 $mA \cdot cm^{-2}$ in 1 M potassium hydroxide (KOH), respectively. In another work, nickel/nickel oxide (Ni-NiO) and cobalt/cobalt oxide (Co-CoO) were chemically synthesized with three-dimensional hierarchical porous graphene (3DHPG) on GCE [24]. Ni-NiO @3DHPG was characterised with an OER onset potential E_{onset} of 1.53 V vs. RHE, η of 164 mV and Tafel of 55 $mV \cdot dec^{-1}$, while Co-CoO@3DHPG revealed an E_{onset} of 1.59 V vs. RHE, η of 168 mV and Tafel of 65 $mV \cdot dec^{-1}$ determined in 1 M KOH. In the work of Xia et al. [20], an efficient OER catalyst of Gr/NiFe layered double hydroxide (LDH) was chemically fabricated on GCE. The catalyst revealed an OER E_{onset} of 1.48 V vs. RHE and η of 250 mV determined in 0.1 M KOH. Improved electron transport was provided by the presence of graphene material in the catalyst structure. Enhanced OER catalytic performance was also obtained for electrodeposited NiFe LDH combined with GO on nickel foam (GO-NiFe-LDH) [12] and NiFe LDH combined with reduced graphene oxide (rGO) on nickel foam (NiFe-LDH/RGO) [21]. The OER η was determined to be 119 mV and 150 mV determined at 10 $mA \cdot cm^{-2}$ in 1 M KOH for GO-NiFe-LDH and NiFe-LDH/RGO/NF, respectively. The efficient

OER was associated with the presence of the electron interaction between the metal and graphene.

The literature presents the possibility of improving OER performance of the electrode by combining Fe-, Ni- and/or Co-based oxides/hydroxides and GO compared to the Ru- and Pt-based catalysts used so far for OER. There is a lack of literature reports presenting some discussions and determining the specific role of the addition of graphene to the state-of-the-art NiFe and/or CoNiFe-based oxide/hydroxides. Moreover, most of the performed studies were focussed mainly on chemically synthesised catalysts, which usually required post-processing and some additives (e.g. Nafion) to form an ink to produce an OER electrode. This in turn significantly affects the final structure and electrocatalytic performance of the electrode.

Therefore, in this work, the influence of the addition of GO to the NiFe and CoNiFe oxides/(oxy)hydroxides catalysts towards OER was studied. The NiFe, CoNiFe, NiFe-GO, and CoNiFe-GO were synthesised by the electrodeposition process directly on nickel foam. The process made it possible to fabricate OER electrodes with reduced GO, and without any additives that could interfere with the structural and electrochemical measurements. The effect of the addition of GO to the NiFe and CoNiFe on their morphological, structural, and OER electrocatalytic properties were studied. The role of the GO and metallic species in the OER electrocatalytic process is discussed.

2. Results

2.1. Electrosynthesis process and morphology of the deposits

The catalysts were synthesised by electrodeposition onto the surface of nickel foam. The chronoamperometric graph recorded during the deposition is presented in Figure 1a.

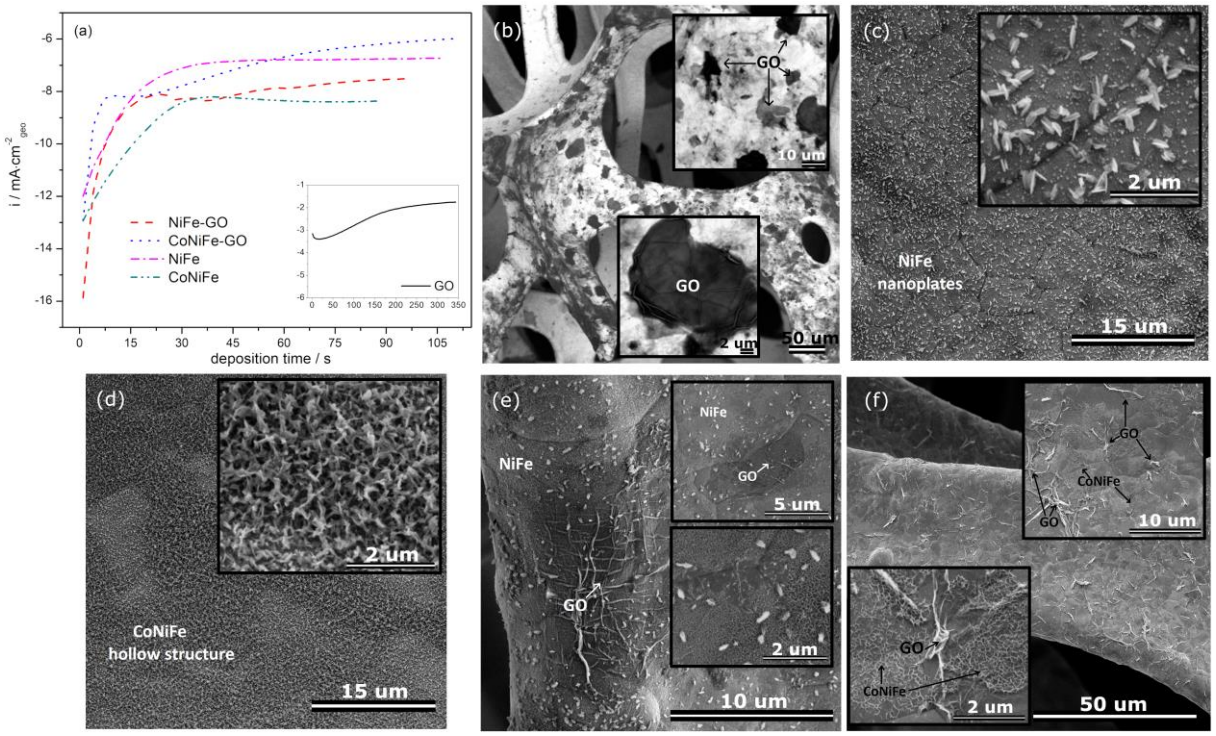

Figure 1. Chronoamperometric graphs recorded during electrochemical deposition of the catalysts on nickel foam (a), SEM images of GO (b), NiFe (c), CoNiFe (d), NiFe-GO (e), and CoNiFe-GO (f) deposited on nickel foam.

Each synthesis (except for GO) began with a fast increase of the cathodic current, which is associated with the formation of the new catalyst phase on the surface of the substrate [25]. Afterwards, the current density tended to stabilize for NiFe and CoNiFe, which may be associated with the steady-state formation of the catalyst film on the metallic surface. The addition of the cobalt species to NiFe resulted in a lower overall current density during the synthesis process. In the case of the deposition of NiFe and CoNiFe on GO/nickel foam, the specific current density peak appeared after around 8 s and 20 s of the deposition for CoNiFe-GO and NiFe-GO, respectively. Because the metallic films were deposited on the surface of nickel foam already modified with GO, the peak may be associated with the reduction process of the already-deposited GO. Afterwards, the current density increased due to the film formation, and then it gradually stabilised over time. A different chronoamperometric trend can

be observed in the case of the electrodeposition of GO on the surface of nickel foam (Figure 1a inset). In this case, the cathodic current density decreased during the first 6 s of the synthesis, then it increased and tended to stabilize. The initial drop of the current density may be related to the preparation (e.g. passivation) of the metallic surface for GO deposition. The latter is a typical process in the case of the electrodeposition of the conductive film on active metals [26].

The morphology of the deposits was analyzed by scanning electron microscopy (SEM) and is presented in Figure 1b–f. Typical GO flakes regularly distributed over the surface of the nickel foam were successfully obtained after the one-step electrodeposition process (Figure 1b). The structure of the NiFe deposited directly on the substrate was characterised with the nanoflake-like morphology that is common for electrodeposited NiFe (oxy)hydroxides/oxides LDH [27]. The structure of the NiFe after the addition of cobalt species (CoNiFe) was characterised with interconnected nanoflakes, which formed a porous 3D structure, uniformly distributed over the entire surface of the nickel foam (Figure 1d). The morphology of the catalysts changed after the combination of GO with NiFe and CoNiFe (Figure 1e,f). In each case, the SEM images clearly show the complete coverage of the surface of the GO/Ni foam with the NiFe or CoNiFe. Less nanoplate-like structures of NiFe could be observed around the GO flakes (Figure 1e). The already deposited GO probably inhibited the formation of Ni- and Fe- species on its surface. Nevertheless, the morphology of the NiFe and GO (Figure 1e) is similar to that observed for each of the singly deposited materials (Figure 1b for GO, Figure 1c for NiFe). Different morphologies can be observed in the case of CoNiFe (Figure 1d) and CoNiFe-GO (Figure 1f). Here, the addition of the GO layer induced much more differences in the morphology of the deposits. Deposition of the CoNiFe on the GO/Ni foam changed the shape of the GO flakes, with some agglomerations visible (Figure 1f). On the other hand, the presence of the GO resulted in the formation of a CoNiFe layer, which only remained an interconnected 3D porous material in some areas.

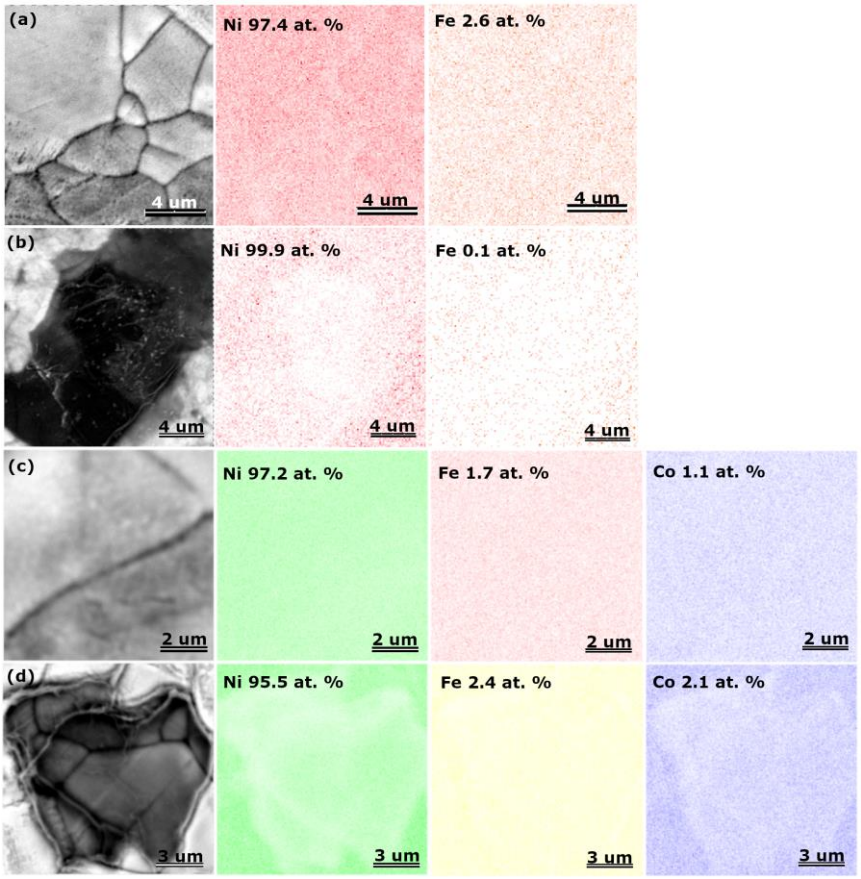

Figure 2. SEM images and corresponding EDX maps of NiFe (a), NiFe-GO (b), CoNiFe (c), and CoNiFe-GO (d) deposited on nickel foam (error ≤ 0.5 at.%).

Figure 2 presents the energy dispersive X-ray (EDX) maps with corresponding SEM images of the catalysts. The analysis confirms the presence of the following elements in the catalyst structure: Ni and Fe for NiFe and NiFe-GO, and Ni, Fe, and Co for CoNiFe and CoNiFe-GO. Since the atomic percentage of iron and cobalt in the catalysts is within the measurement error, it can be stated that their amount is at a similar level, regardless of the type of catalyst. The EDX maps show that deposition of nickel, iron, and cobalt species is preferable on the surface around the graphene oxide flake. The deposited GO probably inhibited the electrodeposition process of NiFe and CoNiFe on its surface. This may be the reason for the slower stabilization of the synthesis current density observed in the chronoamperograms (Figure 1a).

2.2. X-Ray Photoemission Spectroscopy and X-Ray Absorption Spectroscopy analysis of the catalysts

Figure 3 a–d shows the X-ray absorption spectra (XAS) of the L_3 edge of the nickel (a), iron (b), cobalt (c) and carbon (d) of the studied catalysts.

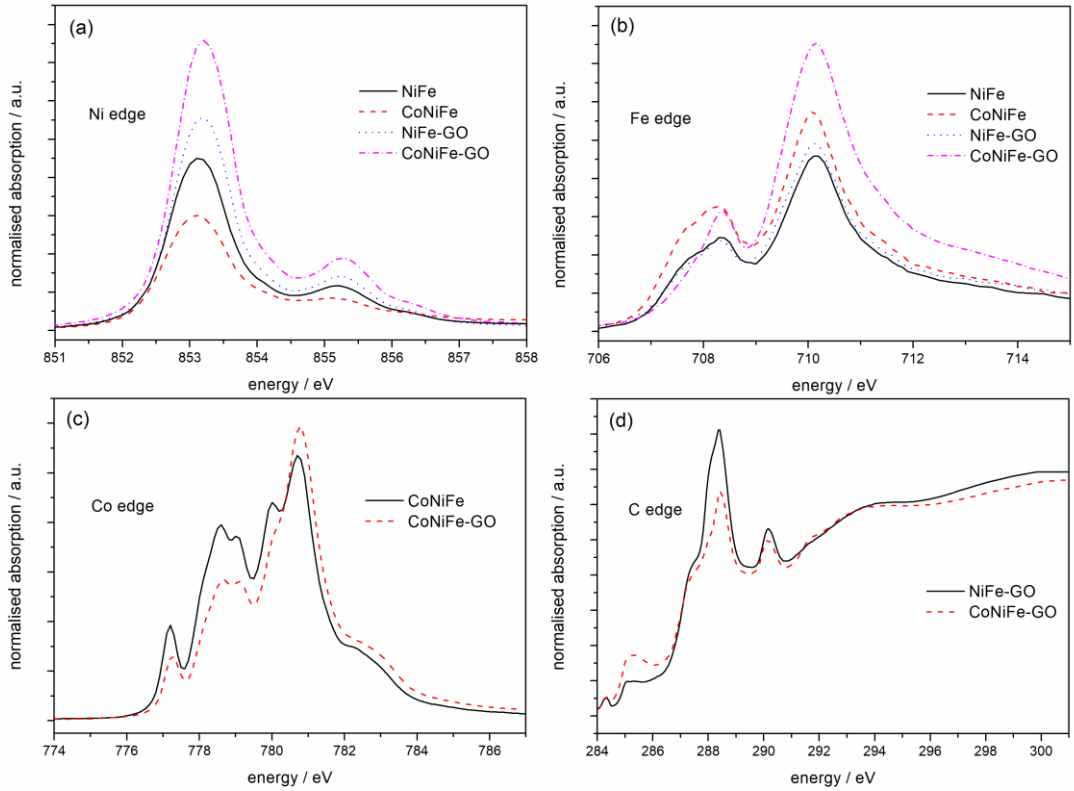

Figure 3. Normalized XAS spectra of NiFe, CoNiFe, NiFe-GO, CoNiFe-GO.

The appearance of a shoulder peak at the L_3 edge of the nickel (Figure 3a) at 855 eV indicates the presence of oxides in the structure of the catalysts (Ni in a strong crystal field) [28,29]. The shape of the XAS spectra (Ni edge) indicates a similar type of oxides in the structure of the catalysts. The addition of the GO to the NiFe and CoNiFe intensified both the nickel and iron L_3 edge peaks, indicating partial electron transfer from the nickel and iron to the substitutional GO (carbon) [30]. In the case of the edge of the iron (Figure 3b), the XAS spectra indicate the presence of iron atoms in the third oxidation state Fe^{3+} in each of the studied catalysts [28,29]. The iron edge peak observed at 707 eV disappeared after the addition of the

GO to the CoNiFe, indicating a change in the structure of the catalyst. However, the type of oxides/hydroxides present in the catalyst structure cannot be determined from the spectra.

The shift of the XAS spectra and the change in its intensity were observed for the L_3 edge of the cobalt after addition of GO into CoNiFe (Figure 3c). The observed changes resulted in charge transfer from the cobalt to the carbon and the formation of the Co-O-C bond in the catalyst [31]. Moreover, the spectra indicate that the dominant cobalt species in the studied catalysts were Co^{3+} and Co^{2+} [25].

The L_3 of the carbon edge in NiFe-GO and CoNiFe-GO is presented in Figure 3d. In general, the absorption edge at ~285.2 eV and ~293.7 eV corresponds to the excitation signal of carbon in the sp^2 network into the π^* band (C=C) and σ* band (C-C), respectively [32,33]. The signals observed at ~287.2 eV (σ*: C-O and/or π^*: C-OH), ~288.4 eV (σ*: C-O), ~290.1 eV (π^*: C=O) and ~291.6 eV (π^*: O-C=O) correspond to a state in which the local sp^2 bonding is influenced mainly by the oxygen functionalization [32,33]. The position of the peak and the intensity of spectra differ for the NiFe-GO and CoNiFe-GO indicating different electronic structures and interactions around the Ni, Fe, Co and GO.

The XPS analysis showed that the addition of cobalt to the NiFe induced the formation of new nickel species, i.e. Ni^{3+}, in the catalyst structure (Figure 4a). The effect of the addition of cobalt to the NiFe on its structure was studied in detail in our previous work [25]. The appearance of Ni^{3+} was also observed after the addition of GO to the NiFe. Both, the GO and the addition of Co to the NiFe resulted in the formation of nickel species in the second and third oxidation states (Ni^{2+}, Ni^{3+}) with the same Ni^{2+}/Ni^{3+} ratio of around 80%/20%. The addition of GO to the CoNiFe did not change the structure of the catalyst concerning the type of the nickel species and the ratio of Ni^{2+}/Ni^{3+} (80%/20%).

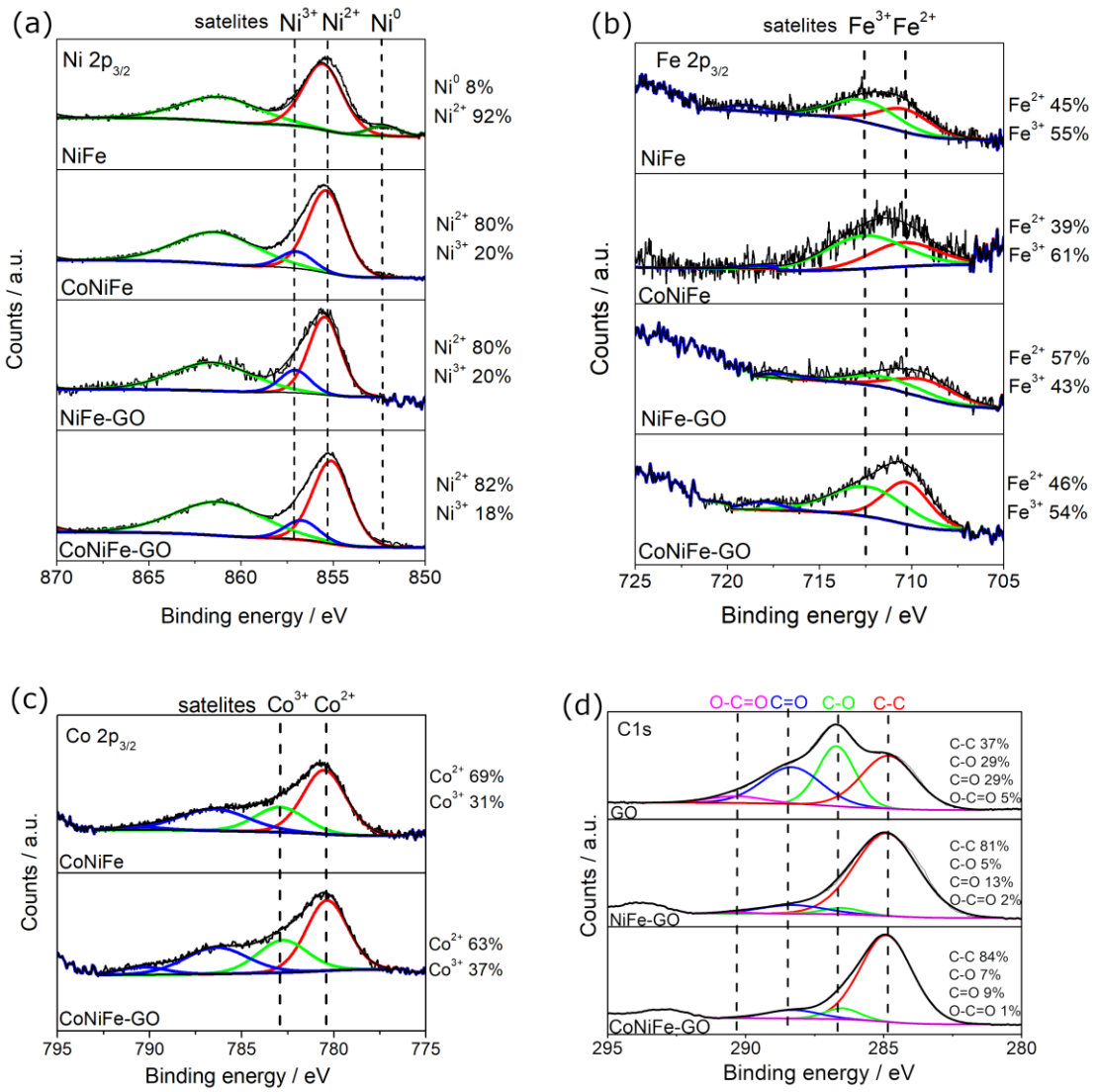

Figure 4. XPS high resolution spectra of Ni2p (a), Fe2p (b), Co2p (c) and C1s (d) regions of the catalysts with the determined surface concentration of the elements (error ≤ 5%).

Two kinds of iron species were found in each of the materials studied i.e., Fe^{2+} and Fe^{3+} (Figure 4b). The Fe^{2+}/Fe^{3+} ratio in the NiFe slightly decreased to 39%/61% from 45%/55% after the addition of the cobalt species. A different situation was observed in the case of the NiFe and CoNiFe catalysts after the addition of GO. The ratio of Fe^{2+}/Fe^{3+} increased from Fe^{2+}(45%)/Fe^{3+}(55%) to Fe^{2+}(57%)/Fe^{3+}(43%) for the NiFe, and from Fe^{2+}(39%)/Fe^{3+}(61%) to Fe^{2+}(46%)/Fe^{3+}(54%) for the CoNiFe. The same type of cobalt species, i.e. Co^{2+} and Co^{3+}, and

virtually the same percentage ratio of Co^{2+}/Co^{3+} remained in the catalyst after the addition of GO to the CoNiFe (Figure 4c).

Figure 4d presents the XPS spectra of the C 1s region of the GO, NiFe-GO, and CoNiFe-GO. The C 1s spectrum of the catalysts indicates the degree of oxidation with four different components corresponding to carbon atoms in different functional groups, i.e. non-oxygenated ring C-C (284.9 eV), the C in C-O (286.6 eV), and C=O (288.5 eV) bonds, and carboxylate carbon O-C=O (290.0 eV), which agrees with the XAS analysis (Figure 3) [34]. The analysis showed that the non-oxygenated ring C is about 37% for the GO, while it increased significantly after combining the GO with the NiFe (81%) or CoNiFe (84%). On the other hand, the percentage of C-O, C=O, and O-C=O decreased down to around 5–7%, 9–13%, and 1–2%, respectively, for the GO-modified catalysts. The latter indicates that most of the oxygen functional group in the GO was removed, and thus the GO present in the structure of the NiFe or CoNiFe is in a reduced form [20]. The analysis confirms that the second step of the electrodeposition process lead to the simultaneous deposition of the NiFe or CoNiFe and the reduction of the GO. A reduced form of GO combined with NiFe was also obtained by others after one-step electrodeposition by cyclic voltammetry [12].

2.3. Electrochemical studies of the catalysts towards OER

The electrochemical performance of the catalysts towards OER was studied in an aqueous solution of 1 M KOH. Figure 5 presents the LSV graphs (a) with the corresponding evolution of OER overpotential (determined at 10 $mA \cdot cm^{-2}$), onset potential E_{onset} (b), and Tafel plots (c).

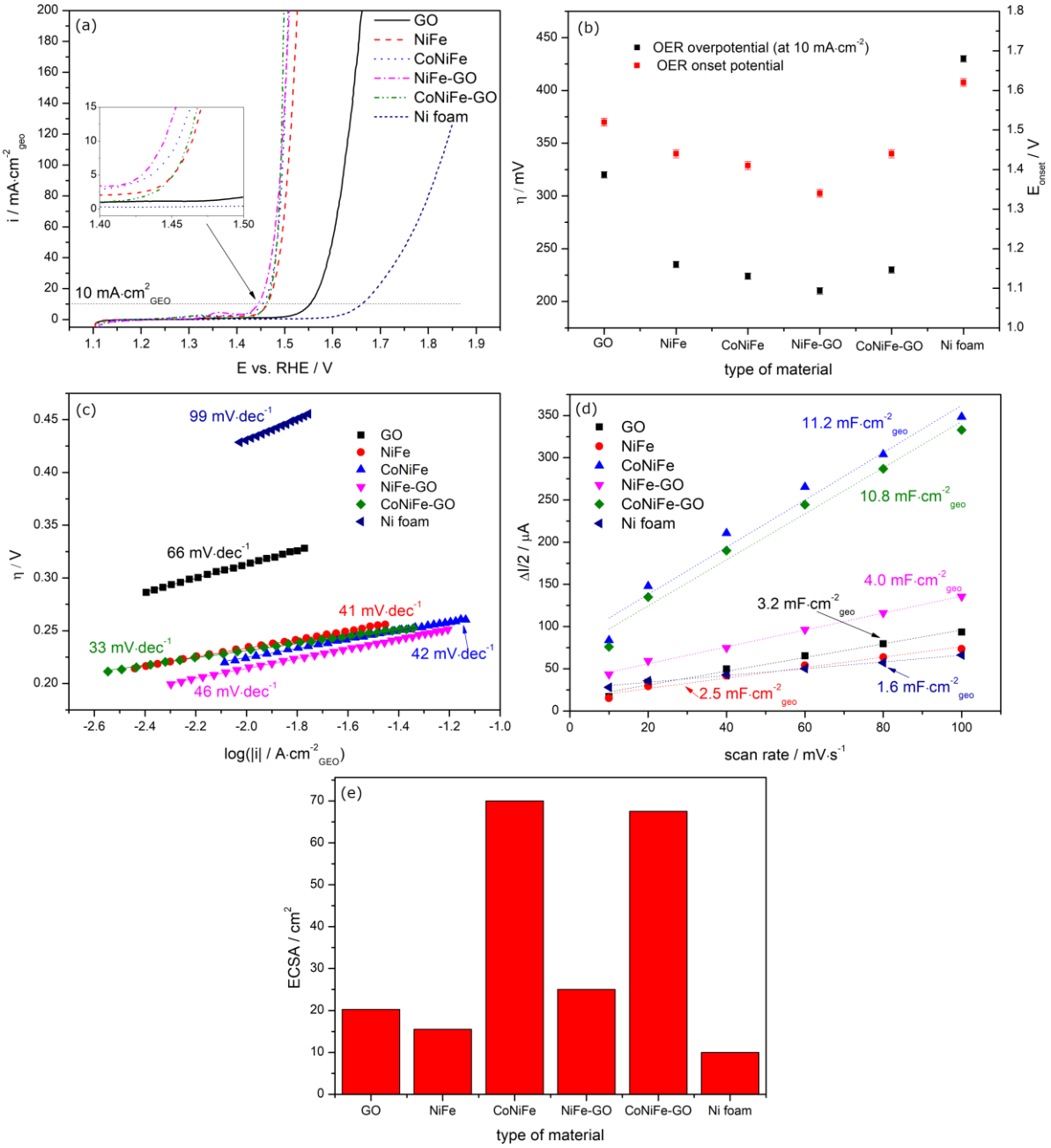

Figure 5. Linear scan voltammetry profiles (a) with corresponding evolution of OER overpotential η (10 mA·cm^{-2}) and onset potential E_{onset} (b), and Tafel plots (c) of the catalysts. Double layer capacitance C_{dl} (d) and corresponding electrochemical active surface area (ECSA) (e) determined for each catalyst.

The LSV graphs show that coating the nickel foam with the catalyst layer resulted in each case in higher catalytic performance of the sample towards OER compared to the bare substrate. The addition of the GO to the NiFe significantly reduced η (10 mA·cm^{-2}) and E_{onset} to 210 mV

and 1.34 V, respectively, compared to GO (η: 320 mV, E_{onset}: 1.52 V) and NiFe (η: 235 mV, E_{onset}: 1.44 V) alone. A difference was observed in the case of the CoNiFe and CoNiFe-GO catalysts. Here, the addition of the GO to the CoNiFe (η: 230 mV, E_{onset}: 1.44 V) significantly increased the OER catalytic activity of the sample compared to GO alone (η: 320 mV, E_{onset}: 1.52 V), but the overall activity of the CoNiFe-GO was lowered compared to CoNiFe alone (η: 224 mV, E_{onset}: 1.41 V).

The catalytic efficiency towards OER can be also assessed by analyzing the Tafel plots of the catalysts (Figure 5c). The Tafel for bare nickel foam was determined to be 99 $mV \cdot dec^{-1}$, which is in agreement with the literature [35,36]. A lower Tafel slope was observed for nickel coated with GO, indicating faster kinetics towards OER compared to the bare substrate [37]. The slopes for the NiFe (41 $mV \cdot dec^{-1}$) and CoNiFe (42 $mV \cdot dec^{-1}$) were similar, which indicates that the same OER catalytic mechanism was in action. The addition of the GO to the NiFe resulted in a slight increase of the slope from 41 to 46 $mV \cdot dec^{-1}$, while the presence of the GO in the CoNiFe led to a decrease in Tafel down to 33 $mV \cdot dec^{-1}$.

Figures 5d and 5e present a linear approximation of the capacitive currents versus scan rate obtained from cyclic voltammograms with the determined double layer capacitance C_{dl} and corresponding ECSA, respectively, for the samples. Coating the nickel foam with the catalysts resulted in each case in an increase of C_{dl} and ECSA compared to the bare substrate. The highest C_{dl}/ECSA was obtained for the CoNiFe: the addition of the cobalt species to the NiFe resulted in an around 4-fold increase in the surface area of the catalyst. The latter was related to the change in the morphology from the nanoplate-like structure typical for NiFe to the nanoplate porous interconnected 3D network typical for CoNiFe (Figure 1). The increase in the surface area of the catalyst after mild doping of NiFe with cobalt was also observed in the literature [38]. The addition of the GO to the CoNiFe left the C_{dl}/ECSA of the material virtually unchanged (slightly lowered) compared to the CoNiFe alone. A difference could be observed

in the case of the GO and NiFe. Here, the surface area of the NiFe increased after adding the GO to its structure. Since the C_{dl}/ECSA of GO (3.2 $mF \cdot cm^{-2}_{geo}$ / 20 cm^2) is higher than for NiFe (2.5 $mF \cdot cm^{-2}_{geo}$ / 15.5 cm^2) alone, it indicates that GO was responsible for the increase in the surface area of the NiFe-GO (4.0 $mF \cdot cm^{-2}_{geo}$ / 25.0 cm^2). The virtual lack of change in the CoNiFe-GO surface area and the change of the surface for the NiFe-GO compared to the catalysts alone may be due to their corresponding change in the morphology observed in the SEM images (Figure 1).

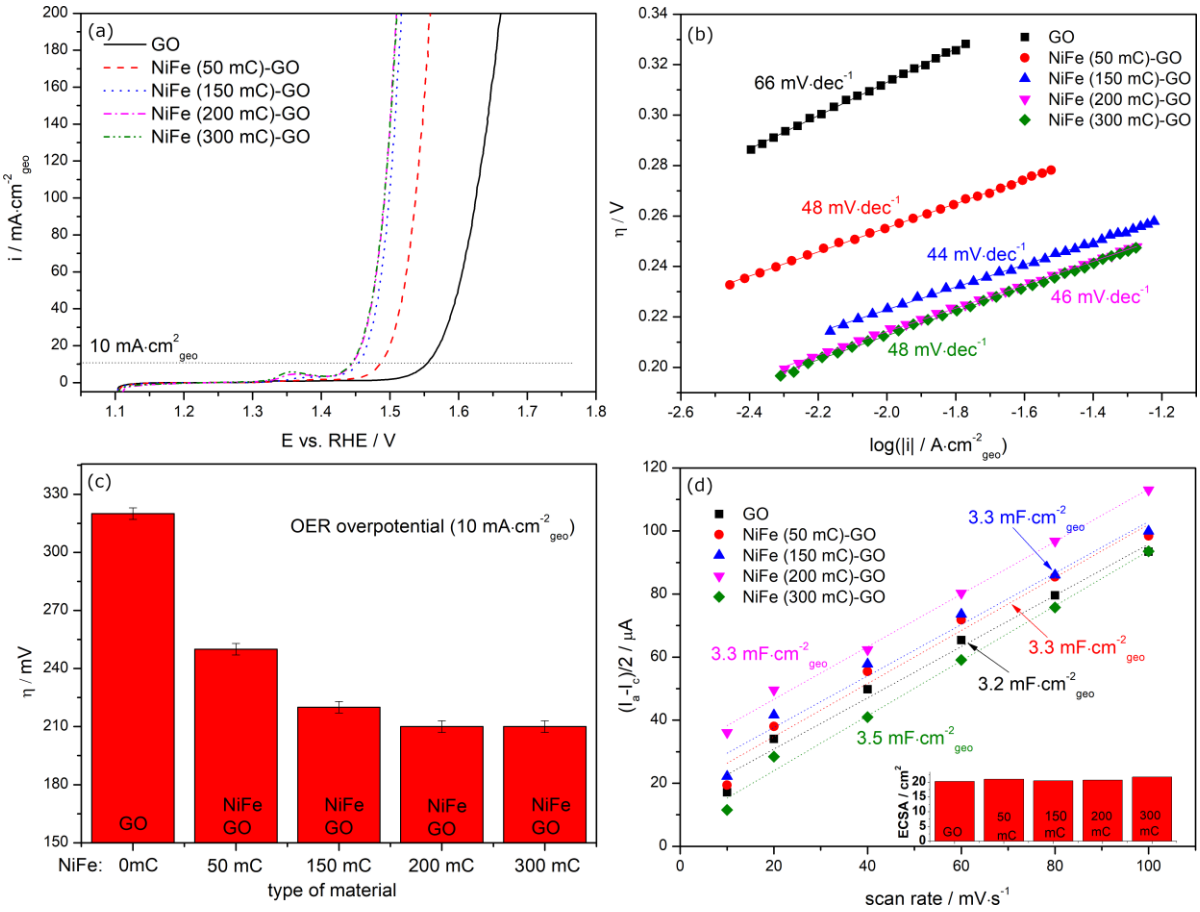

Figure 6. Linear scan voltammetry profiles (a) with corresponding Tafel plots (b) and evolution of OER overpotential η(10 $mA \cdot cm^{-2}$) (c), and C_{dl}, ECSA (d) of the catalysts.

Since the NiFe-GO revealed the highest catalytic activity towards OER compared to the NiFe and GO alone, and the other catalysts, the further electrochemical studies focussed on this material. Figures 6 and 7 present the effect of the change in the electrodeposition charge Q_{dep}

of the NiFe in the NiFe-GO and the GO in the NiFe-GO, respectively, on their electrocatalytic performance towards OER and C_{dl}/ECSA. The LSV profiles of the NiFe (Q_{dep}: 50–200 mC)-GO recorded in an aqueous solution of 1 M KOH and the corresponding evolution of the OER overpotentials are presented in Figure 6a and 6c, respectively. The graphs clearly show that the OER overpotential decreases with a higher deposition charge of NiFe, which is valid for $Q_{dep} \leq$ 200 mC. The lowest $\eta(10\ mA \cdot cm^{-2})$ equaling 210 mV was obtained for the NiFe(200 mC)-GO, while the highest $\eta(10\ mA \cdot cm^{-2})$ of 250 mV was for the NiFe(50 mC)-GO. The corresponding Tafel slope reveals a similar trend as the OER η i.e., the higher the Q_{dep} of the NiFe in the NiFe-GO, the lower the slope (valid for $Q_{dep} < 200$ mC). Any change or deterioration of the OER catalytic activity of the NiFe-GO for $Q_{dep} > 200$ mC may be due to the overgrow of deposited NiFe, which begins to block the ions and electron transport. The latter can also be confirmed by the Tafel analysis, i.e. the slopes for the NiFe(300 mC)-GO begin to rise quickly, which indicates a change in the OER kinetics due to the slowed exchange of ions and electrons. The connection of the GO with the NiFe resulted in a slight increase of the C_{dl}/ECSA compared to the GO and NiFe alone (Figure 5d,e). However, Figure 6d shows that this change is further independent of the NiFe deposition charge. A difference was observed for the GO in the NiFe-GO (Figure 7). The OER η for the NiFe-GO(100–300 mC) decreased as the Q_{dep} of the GO increased, which was valid for $Q_{dep} \leq 200$ mC. A higher deposition charge of the GO in the NiFe-GO resulted in a re-increased of the OER η up to 233 mV, which was due to the overgrowth of the GO over the NiFe, which was characterised by a significantly higher C_{dl}/ECSA of $7.0\ mF \cdot cm^{-2}/44.0\ cm^2$ compared to the rest of the samples.

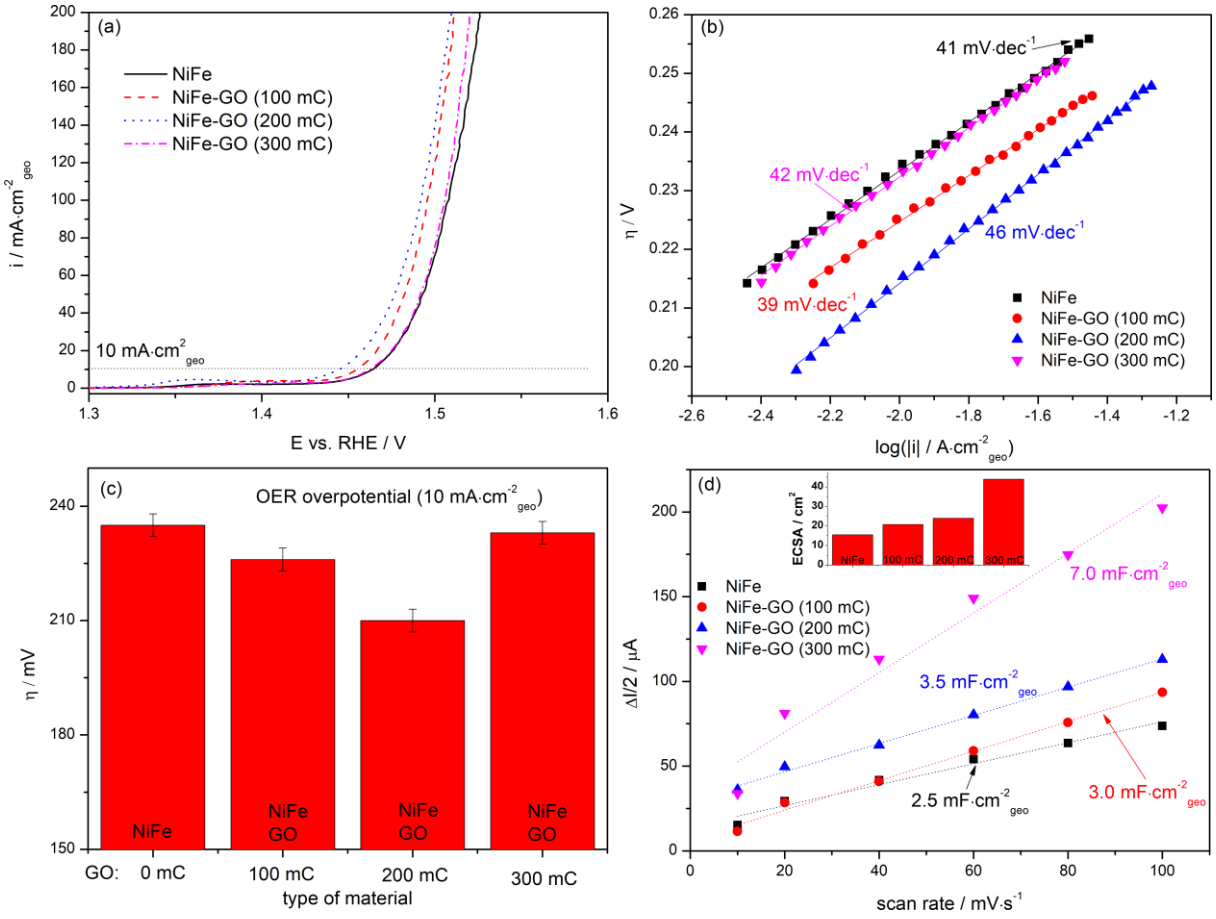

Figure 7. Linear scan voltammetry profiles (a) with corresponding Tafel plots (b) and evolution of OER overpotential η (±3 mV) (c), and C_{dl}, ECSA (d) of the catalysts.

This, in turn, resulted in blocking of the catalyst surface and the ion/electron transport became inhibited. The C_{dl}/ECSA for the NiFe-GO(100–300 mC) progressively increased as the deposition charge of the GO in the NiFe-GO increased, which was a different trend compared to the NiFe(50–300 mC)-GO. Because of this, the data indicate that the improvement in the OER of the NiFe-GO with the higher Q_{dep} of the NiFe and GO resulted mainly from the NiFe structure and the GO electroactive surface area/porosity, respectively.

3. General discussion

The studies showed that the addition of GO to the NiFe and CoNiFe by the electrodeposition technique significantly affected their morphological, structural, and electroactivity towards OER. The addition of GO to NiFe resulted in a significant increase in their OER catalytic

performance compared to GO and NiFe alone. The OER η(10 $mA \cdot cm^{-2}$) and E_{onset} were reduced down to 210 mV and 1.34 V, respectively, compared to GO (η: 320 mV, E_{onset}: 1.52 V) and NiFe (η: 235 mV, E_{onset}: 1.44 V). A difference was observed for the CoNiFe-GO, i.e. here, the overall OER catalytic activity (η: 230 mV, E_{onset}: 1.44 V) increased compared to GO alone, however, it was reduced in comparison with the CoNiFe (η: 224 mV, E_{onset}: 1.41 V). The phenomena can be associated with several factors. First, the morphology which was changed when CoNiFe was combined with GO (Figure 1f). The morphology of the CoNiFe-GO was characterised by a non-uniformly distributed 3D nanostructure of CoNiFe and some agglomerations of GO microflakes, which was not the case for GO and CoNiFe alone (Figure 1b and 1d, respectively). A difference was observed for the NiFe-GO, i.e. the morphology of the GO and NiFe remained virtually the same as it was before the connections of the catalysts.

Another factor influencing the OER performance of the combined catalysts is structure. The combination of GO with NiFe or CoNiFe resulted in the same oxidation state of the nickel, iron, and cobalt appearing in their structure (Figure 4). The addition of GO induced the formation of Ni^{3+} in the NiFe-GO, so the final percentage ratio of nickel Ni^{2+}/Ni^{3+} in each of the studied catalysts became virtually the same (80%/20%) (Figure 4a). On the other hand, the presence of GO induced the formation of Fe^{2+} in each of the catalysts, thus the ratio of Fe^{2+}/Fe^{3+} in NiFe/CoNiFe-GO increased compared to the NiFe and CoNiFe. Moreover, it differed depending on the type of the catalyst i.e., 57%/43% for the NiFe-GO and 46%/54% for the CoNiFe-GO.

XAS analysis indicated the change in an electronic structure of the catalysts after the addition of GO (Figure 3). The analysis showed that the electronic structure around the nickel and iron was changed, which may be associated with interactions between the NiFe and CoNiFe with the GO (carbon domains). Something similar was observed in the case of the addition of N-doped nanocarbon to the NiFe [16]. To summarize, the disturbed morphology and change in

the electronic structure of the CoNiFe after the addition of GO could result in a less attractive OER catalytic activity of this material compared to CoNiFe alone or NiFe-GO.

The further OER studies on the NiFe-GO showed that apart from their resulting desirable morphology and structure, each of the material forming the catalyst has a specific role in influencing the OER process. The improvement in the OER with the increasing Q_{dep} of the catalysts resulted mainly from the structure of the NiFe (change of the Q_{dep} did not influence the ECSA, while the OER activity increased) and from the electroactive surface area of the GO (higher Q_{dep} resulted in a gradual increase of the ECSA and OER activity).

4. Conclusions

The effect of the addition of GO to electrodeposited NiFe and CoNiFe on their morphological, structural, and OER catalytic performance was studied successfully. The studies showed that modification of NiFe or CoNiFe with GO resulted in the significant change of their structure, morphology, and OER activity. The changes differed depending on the presence of cobalt in the catalyst's structure. The combination of GO with NiFe led to the formation of a uniformly deposited catalyst characterised by GO microflakes and NiFe nanoplates with higher C_{dl}/ECSA (4.0 mF·cm^{-2}/25.0 cm^2) and OER activity (η: 210 mV, E_{onset}: 1.34 V) compared to NiFe (C_{dl}: 2.5 mF·cm^{-2}, ECSA: 15.5 cm^2, η: 235 mV, E_{onset}: 1.44 V) and GO (C_{dl}: 3.2 mF·cm^{-2}, ECSA: 20.2 cm^2, η: 320 mV, E_{onset}: 1.52 V) alone. On the other hand, the addition of GO to CoNiFe induced agglomerations of graphene flakes, which results in slightly lower C_{dl}/ECSA (10.8 mF·cm^{-2}/67.5 cm^2) and reduced OER activity (η: 230 mV, E_{onset}: 1.44 V) compared to CoNiFe (C_{dl}: 11.2 mF·cm^{-2}, ECSA: 70 cm^2, η: 224 mV, E_{onset}: 1.41 V) alone. Further electrochemical studies on the most efficient catalyst, i.e. NiFe-GO, showed that a significant improvement in the OER catalytic activity was obtained from its specific structure, morphology, and electroactive surface area obtained after the combination of NiFe and GO. It

should be note that the main influence on the greater OER catalytic activity was the structure of NiFe and the electroactive surface area of GO.

5. Experimental

5.1. Fabrication of the catalysts

NiFe and CoNiFe oxides/(oxy)hydroxides were synthesised in a one-step process by electrodeposition at -1.1 V vs. Ag/AgCl in an aqueous solution of 4 mM nickel (II) nitrate hexahydrate ($Ni(NO_3)_2 \cdot 6H_2O$) (98%, Sigma Aldrich), 4 mM iron (III) nitrate nonahydrate ($Fe(NO_3)_3 \cdot 6H_2O$) (98%, Sigma Aldrich), and 0 or 4 mM cobalt (II) nitrate hexahydrate ($Co(NO_3)_2 \cdot 6H_2O$) (98%, Sigma Aldrich) at 25°C. NiFe-GO and CoNiFe-GO were fabricated in a two-step process: (1) electrodeposition of GO performed at -1.0 V vs. Ag/AgCl in an aqueous solution of 4.4 $mg \cdot ml^{-1}$ GO (Graphene Supermarket) at 25°C; (2) electrodeposition of NiFe or CoNiFe carried out at -1.1 V vs. Ag/AgCl in an aqueous solution of 4 mM $Ni(NO_3)_2 \cdot 6H_2O$, 4 mM $Fe(NO_3)_3 \cdot 6H_2O$, and 0 or 2 mM $Co(NO_3)_2 \cdot 6H_2O$ at 25°C. Unless otherwise stated, the deposition time was limited to a charge of 200 mC for each deposition process. The deposition parameters, i.e., the concentration of each metal nitrate and deposition charge, were optimised concerning the most efficient OER performance of the Ni-, Fe- and Co-based catalyst obtained in the previous work [25].

The electrodeposition process was performed in a one-compartment water-jacketed cell controlled by a potentiostat (VersaSTAT 4). The working electrode (WE) was nickel foam or foil with an exposed area of 0.25 cm^2. Before each deposition process, the substrates were cleaned ultrasonically in distilled water (5 minutes) and acetone (5 minutes), respectively. The reference and counter electrodes were Ag/AgCl (4M KCl) and platinum mesh, respectively. Distilled water was used for the solutions. The measurement temperature was controlled by a thermostat (Julabo F12).

5.2. Characterisations

The morphology and structure of the catalysts were characterised by a scanning electron microscope (FEI QUANTA FEG 250) with energy dispersive X-ray (EDX). X-ray absorption spectroscopy (XAS) was performed at the 04BM beamline at the National Synchrotron Radiation Centre SOLARIS [39]. The spectra were obtained using the Total electron yield (TEY) detection mode which can sample down to a depth of a few nanometers at room temperature. The beamline optics was optimised to perform the experiment with an energy resolution of 200 meV and better. X-ray photoemission spectra (XPS) of the catalysts were obtained on an ultra-high vacuum spectrophotometer at a pressure below 1.1 $x10^{-8}$ mBar at room temperature (Omicron NanoTechnology). Photoelectrons were detected by a spectrophotometer equipped with a 128-channel collector. The X-ray anode was operated at 15 keV and 300 W. The chemical composition calculations were determined based on the survey spectra collected in a wide range of binding energies, while valence state calculations were based on the high-resolution spectra. The C1s peak (285.0 eV) was used to correct the results. Analysis of XPS spectra was performed with the Casa-XPS software using a Gaussian–Lorentzian (GL30) curve as a fitting algorithm and a Shirley background subtraction.

5.3. Electrochemical studies

The setup for the electrochemical studies was the same as for the catalyst's fabrication (section 2.1.) with some exceptions: the working electrode was coated or bare nickel foam with an exposed area of 0.25 cm^2, while the reference electrode was a reversible hydrogen electrode (RHE) (Gaskatel). The electrochemical cell was purged with argon 20 minutes before each experiment. The measurements were performed in an aqueous solution of 1 M KOH (Stanlab, pH ≈ 13.9). Before each electrochemical experiment, the electrode was stabilised during cyclic voltammetry (CV) by sweeping the potential from 1.1 to 1.6 V vs. RHE for at least 20 cycles with a scan rate of 100 $mV \cdot s^{-1}$. Linear scan voltammetry (LSV) was performed from 1.1 to 2 V vs. RHE with a scan rate of 5 $mV \cdot s^{-1}$. The recorded current values were normalized by the

geometric area of the nickel electrode (0.25 cm^2). All of the potentials were iR-corrected. The equation: $\eta = E\ (10\ mA \cdot cm^{-2}) - 1.23$ V (vs. RHE) was used to determine the OER overpotential (η) [40]. The double-layer capacitance (C_{dl}) was determined based on CV measurements, which were carried out within the potentials 0.15–0.25 V vs. Ag/AgCl with a scan rate of 10, 20, 40, 60, 80, and 100 $mV \cdot s^{-1}$. The following equation was used to determine C_{dl} from the CV: $C_{dl} = i_{dl} \cdot (2\upsilon)^{-1} = (i_a - i_c) \cdot (2\upsilon)^{-1}$, where υ is the scan rate; i_a and i_c are the anodic and cathodic current densities, respectively; and i_{dl} is the double-layer current density. The electrochemical surface area (ECSA) was calculated based on the following equation $ECSA = C_{dl} \cdot A \cdot C_{spec}^{-1}$, where A represents the geometric surface area of the sample and C_{spec} is the constant specific capacitance of 0.04 $mF \cdot cm^{-2}_{geo}$, which is typical for a metallic-based electrode in an aqueous alkaline solution [41]. Each electrochemical experiment was performed a minimum of three times, and the average of these is presented in the manuscript.

Acknowledgements

This work was supported by the "Nanocrystalline ceramic materials for efficient electrochemical energy conversion" project carried out within the First TEAM programme of the Foundation for Polish Science (grant agreement nr. POIR.04.04.00-00-42E9/17-00). K. Cysewska acknowledges the Polish Ministry of Education and Science for the stipend of the Minister of Science and Higher Education for outstanding young scientists. This publication was developed under the provision of the Polish Ministry of Education and Science project: "Support for research and development with the use of research infrastructure of the National Synchrotron Radiation Centre SOLARIS" under contract nr 1/SOL/2021/2. We acknowledge SOLARIS Centre for the access to the Beamline [XAS], where the measurements were performed.

References

(1) Dehghanimadvar, M.; Shirmohammadi, R.; Sadeghzadeh, M.; Aslani, A.; Ghasempour, R. Hydrogen Production Technologies: Attractiveness and Future Perspective. *International Journal of Energy Research*. John Wiley and Sons Ltd September 1, 2020, pp 8233–8254. doi:10.1002/er.5508

(2) Hosseini, S. E.; Wahid, M. A. *Renewable and Sustainable Energy Reviews* **2016**, *57*, 850–866. doi:10.1016/j.rser.2015.12.112

(3) David, M.; Ocampo-Martínez, C.; Sánchez-Peña, R. Advances in Alkaline Water Electrolyzers: A Review. *Journal of Energy Storage*. Elsevier Ltd June 1, 2019, pp 392–403. doi:10.1016/j.est.2019.03.001

(4) Bodner, M.; Hofer, A.; Hacker, V. *Wiley Interdiscip Rev Energy Environ* **2015**, *4*, 365–381. doi:10.1002/wene.150

(5) Jiang, S.; Ithisuphalap, K.; Zeng, X.; Wu, G.; Yang, H. *J Power Sources* **2018**, *399*, 66–75. doi:10.1016/j.jpowsour.2018.07.074

(6) Zhou, Q.; Chen, Y.; Zhao, G.; Lin, Y.; Yu, Z.; Xu, X.; Wang, X.; Kun Liu, H.; Sun, W.; Xue Dou, S. **2018**, *8*, 5382–5390. doi:10.1021/acscatal.8b01332

(7) Kim, Y. K.; Kim, J. H.; Yim, §; Jo, H.; Lee, J. S. *ACS Catal* **2019**, *9*, 9650–9662. doi:10.1021/acscatal.9b02701

(8) Huang, C.; Zhong, Y.; Chen, J.; Li, J.; Zhang, W.; Zhou, J.; Zhang, Y.; Yu, L.; Yu, Y. *Chemical Engineering Journal* **2021**, *403*, 126304. doi:10.1016/j.cej.2020.126304

(9) Liu, Y.; Zhou, D.; Deng, T.; He, G.; Chen, A.; Sun, X.; Yang, Y.; Miao, P. *ChemSusChem* **2021**, *14*, 5359–5383. doi:10.1002/CSSC.202101898

(10) Gong, L.; Koh, J.; Yeo, B. S. *ChemSusChem* **2018**, *11*, 3790–3795. doi:10.1002/CSSC.201801639

(11) Boumeriame, H.; Da Silva, E. S.; Cherevan, A. S.; Chafik, T.; Faria, J. L.; Eder, D. *Journal of Energy Chemistry* **2022**, *64*, 406–431. doi:10.1016/J.JECHEM.2021.04.050

(12) Han, X.; Suo, N.; Chen, C.; Lin, Z.; Dou, Z.; He, X.; Cui, L. *Int J Hydrogen Energy* **2019**, *44*, 29876–29888. doi:10.1016/j.ijhydene.2019.09.116

(13) Wu, Z.; Li, P.; Qin, Q.; Li, Z.; Liu, X. *Carbon N Y* **2018**, *139*, 35–44. doi:10.1016/j.carbon.2018.06.028

(14) Rezaei, B.; Jahromi, A. R. T.; Ensafi, A. A. *Electrochim Acta* **2016**, *213*, 423–431. doi:10.1016/j.electacta.2016.07.133

(15) Mahale, N. K.; Ingle, S. T. *Energy* **2017**, *119*, 872–878. doi:10.1016/j.energy.2016.11.053

(16) Yin, S.; Tu, W.; Sheng, Y.; Du, Y.; Kraft, M.; Borgna, A.; Xu, R. *Advanced Materials* **2018**, *30*, 1705106. doi:10.1002/ADMA.201705106

(17) Wu, S.; Shen, X.; Zhu, G.; Zhou, H.; Ji, Z.; Ma, L.; Xu, K.; Yang, J.; Yuan, A. *Carbon N Y* **2017**, *116*, 68–76. doi:10.1016/J.CARBON.2017.01.085

(18) Zhang, X.; Li, X.; Wang, W.; Yang, Z. *Surf Sci* **2022**, *717*, 122000. doi:10.1016/J.SUSC.2021.122000

(19) Zhou, A.; Bai, J.; Hong, W.; Bai, H. *Carbon N Y* **2022**, *191*, 301–332. doi:10.1016/J.CARBON.2022.01.056

(20) Xia, D. C.; Zhou, L.; Qiao, S.; Zhang, Y.; Tang, D.; Liu, J.; Huang, H.; Liu, Y.; Kang, Z. *Mater Res Bull* **2016**, *74*, 441–446. doi:10.1016/j.materresbull.2015.11.007

(21) Li, C.; Chen, J.; Wu, Y.; Cao, W.; Sang, S.; Wu, Q.; Liu, H.; Liu, K. Enhanced Oxygen Evolution Reaction Activity of NiFe Layered Double Hydroxide on Nickel Foam-Reduced Graphene Oxide Interfaces. *International Journal of Hydrogen Energy*. Elsevier Ltd January 28, 2019, pp 2656–2663. doi:10.1016/j.ijhydene.2018.11.167

(22) Cysewska, K.; Rybarczyk, M. K.; Cempura, G.; Karczewski, J.; Łapiński, M.; Jasinski, P.; Molin, S. *Materials* **2020**, *13*, 2662. doi:10.3390/ma13112662

(23) Tareen, A. K.; Priyanga, G. S.; Khan, K.; Pervaiz, E.; Thomas, T.; Yang, M. *ChemSusChem* **2019**, *12*, 3941–3954. doi:10.1002/CSSC.201900553

(24) Ullah, N.; Zhao, W.; Lu, X.; Oluigbo, C. J.; Shah, S. A.; Zhang, M.; Xie, J.; Xu, Y. *Electrochim Acta* **2019**, *298*, 163–171. doi:10.1016/j.electacta.2018.12.053

(25) Cysewska, K.; Zając, M.; Łapiński, M.; Karczewski, J.; Rybarczyk, M. K.; Kamecki, B.; Jasiński, P.; Molin, S. *Energy Technology* **2021**, *9*, 2100688. doi:10.1002/ENTE.202100688

(26) Tseluikin, V.; Dzhumieva, A.; Yakovlev, A.; Mostovoy, A.; Lopukhova, M. *Crystals (Basel)* **2021**, *11*, 415. doi:10.3390/CRYST11040415

(27) Jin, J.; Xia, J.; Qian, X.; Wu, T.; Ling, H.; Hu, A.; Li, M.; Hang, T. *Electrochim Acta* **2019**, *299*, 567–574. doi:10.1016/J.ELECTACTA.2019.01.026

(28) de Groot, F.; Kotani, A. *Core Level Spectroscopy of Solids*; 2008

(29) de Groot, F. M. F.; Fuggle, J. C.; Thole, B. T.; Sawatzky, G. A. *Phys Rev B* **1990**, *42*, 5459–5468. doi:10.1103/PhysRevB.42.5459

(30) Jiang, J.; Sun, F.; Zhou, S.; Hu, W.; Zhang, H.; Dong, J.; Jiang, Z.; Zhao, J.; Li, J.; Yan, W.; Wang, M. *Nature Communications 2018 9:1* **2018**, *9*, 1–12. doi:10.1038/s41467-018-05341-y

(31) Leng, M.; Huang, X.; Xiao, W.; Ding, J.; Liu, B.; Du, Y.; Xue, J. *Nano Energy* **2017**, *33*, 445–452. doi:10.1016/J.NANOEN.2017.01.061

(32) Gandhiraman, R. P.; Nordlund, D.; Javier, C.; Koehne, J. E.; Chen, B.; Meyyappan, M. *Journal of Physical Chemistry C* **2014**, *118*, 18706–18712. doi:10.1021/JP503941T

(33) de Jesus, L. R.; Dennis, R. v.; Depner, S. W.; Jaye, C.; Fischer, D. A.; Banerjee, S. *Journal of Physical Chemistry Letters* **2013**, *4*, 3144–3151. doi:10.1021/JZ401717J/SUPPL_FILE/JZ401717J_SI_001.PDF

(34) Al-Gaashani, R.; Najjar, A.; Zakaria, Y.; Mansour, S.; Atieh, M. A. *Ceram Int* **2019**, *45*, 14439–14448. doi:10.1016/J.CERAMINT.2019.04.165

(35) Yang, Z.; Zhang, J.-Y.; Liu, Z.; Li, Z.; Lv, L.; Ao, X.; Tian, Y.; Zhang, Y.; Jiang, J.; Wang, C. **2017**, *9*, 40351–40359. doi:10.1021/acsami.7b14072

(36) Zhang, J.; Wang, T.; Liu, P.; Liao, Z.; Liu, S.; Zhuang, X.; Chen, M.; Zschech, E.; Feng, X. *Nat Commun* **2017**, *8*, 15437. doi:10.1038/ncomms15437

(37) Yan, F.; Guo, D.; Kang, J.; Liu, L.; Zhu, C.; Gao, P.; Zhang, X.; Chen, Y. *Electrochim Acta* **2018**, *283*, 755–763. doi:10.1016/j.electacta.2018.06.202

(38) Ullah, H.; Loh, A.; Trudgeon, D. P.; Li, X. *ACS Omega* **2020**, *5*, 20517–20524. doi:10.1021/acsomega.0c02679

(39) Zając, M.; Giela, T.; Freindl, K.; Kollbek, K.; Korecki, J.; Madej, E.; Pitala, K.; Kozioł-Rachwał, A.; Sikora, M.; Spiridis, N.; Stępień, J.; Szkudlarek, A.; Ślęzak, M.; Ślęzak, T.; Wilgocka-Ślęzak, D. *Nucl Instrum Methods Phys Res B* **2021**, *492*, 43–48. doi:10.1016/j.nimb.2020.12.024

(40) Yu, J.; Zhong, Y.; Zhou, W.; Shao, Z. *J Power Sources* **2017**, *338*, 26–33. doi:10.1016/j.jpowsour.2016.11.023

(41) McCrory, C. C. L.; Jung, S.; Peters, J. C.; Jaramillo, T. F. *J Am Chem Soc* **2013**, *135*, 16977–16987. doi:10.1021/ja407115p